

Phase Estimation from Amplitude Collapse in Correlated Matter-Wave Interference

Daniel Derr^{1*†}, Dominik Pfeiffer^{1†}, Ludwig Lind¹,
Gerhard Birkl^{1,2}, and Enno Giese¹

¹Technische Universität Darmstadt, Institut für Angewandte Physik,
Schloßgartenstraße 7, 64289 Darmstadt, Germany.

²Helmholtz Forschungsakademie Hessen für FAIR (HFHF),
GSI Helmholtzzentrum für Schwerionenforschung, 64291 Darmstadt, Germany.

*Corresponding author. Email: daniel.derr@physik.tu-darmstadt.de and daniel.derr@gmx.net

†These authors contributed equally to this work.

Operating matter-wave interferometers as quantum detectors for fundamental physics or inertial sensors in real-world applications with unprecedented accuracies relies on noise rejection, often implemented by correlating two sensors. Such sensors can be spatially separated (gradiometry or gravitational-wave detection) or consist of different internal states (magnetometry or quantum clock interferometry), in which case a signal-amplitude modulation may serve as a signature of a differential phase. In this work, we introduce Phase Estimation from Amplitude Collapse (PEAC) by applying targeted fitting methods for different magnetically sensitive substates of an atom interferometer. We demonstrate that PEAC provides higher trueness (up to 80 % bias reduction) than standard tools for perfectly correlated signals. At its working point near, but not exactly at phase settings resulting in vanishing amplitude, it achieves precision competitive with standard methods, contrasting prior claims of optimal operation at vanishing amplitude. PEAC presents a generally applicable complementary evaluation method for correlated interferometers without phase stability, increasing the overall accuracy and enabling applications beyond atom interferometry.

1 INTRODUCTION

To exploit the full potential of atom interferometers as quantum sensors at the highest accuracy, the signal of interest is often encoded in the differential phase θ between two correlated interferometers. This strategy suppresses common-mode noise and is an established, yet crucial tool for high-precision measurements, e. g. setting new records in the determination of the fine-structure constant (1, 2), forming the working principle of quantum-based gravitational-wave or dark-matter detectors (3–5) on large baselines (5, 6), and being central to operational and proposed quantum tests of fundamental physics (7–10) and general relativity (11–18). It is also key for robust sensors (19, 20) used in magnetometry (21–24), gyroscopy (25–28), or gradiometry (29–31) with applications in inertial sensing, exploration, and navigation (27, 32). In such real-world applications, the differential phase can be extracted even in noisy environments, where the interference signal cannot be resolved in a single interferometer.

However, differential phase estimation in correlation measurements poses its own challenges even for established techniques like fitting ellipses to parametric plots of noisy, but correlated bivariate data which extract the phase from the ellipses' eccentricity (33–36). While usually *precise*, ellipse-based phase estimation is only *accurate* for a circle ($\theta = \pi/2$ and odd multiples). For all other cases, the extracted phase is biased with a systematic error, where the *trueness* of the phase estimation suffers severely at degeneracy points ($\theta = \pi\mathbb{Z}$) at which the ellipse collapses to a line. *Trueness* is a measure for the closeness of the measured to the true phase value as quantified by a bias or systematic error, *precision* is a measure for the spread of controlled repeated estimates, and *accuracy*, though qualitatively, is their combination (37, 38).

In this work, we propose and implement phase estimation from amplitude collapse (PEAC) as an additional, complementary statistical technique for correlated noisy matter-wave interferometers. We demonstrate experimentally and theoretically that PEAC enhances the trueness by a bias reduction of up to 80 % compared to ellipse fitting, albeit at the cost of precision, yielding overall improved accuracy especially near the degeneracy points, i. e. for perfectly in-phase or π -phase-shifted correlated interferometers.

PEAC is inspired by quantum clock interferometry (39–44), where a superposition of internal states undergoes an atom-interferometer sequence, creating a spatial superposition in which pos-

sible relativistic (45, 46) and proper-time effects (47) encode a signal-amplitude loss associated with which-path information (48). Like those schemes, PEAC does not require measuring correlated interferometers individually, but relies on the detection of (possibly incoherent) mixtures of them. A differential phase shift between the individual interferometers induces a beating of their superposed interference fringes. This characteristic structure manifests as collapses and revivals of the combined signal’s oscillation amplitude, whose pattern appears in statistical histograms of population measurements, extractable (32, 49–51) even when suffering large phase noise.

We analyse the PEAC performance in atom interferometers containing a stochastic mixture of magnetically sensitive substates in order to estimate the acceleration induced by a magnetic-field gradient. Using state-selective measurements, we compare this technique to corresponding ellipse fits, demonstrating that PEAC provides a complementary statistical analysis of existing correlation data not through joint phase fitting, but via an optimally chosen transformation of the bivariate coordinates and their amplitude marginal distributions. PEAC demonstrates improved overall performance, with the highest accuracy for phases near, but not exactly at degeneracy points. This working point, where the signal amplitude is small but still finite, contrasts the geometric phase amplification (52) predicted when neglecting the vanishing oscillation amplitude at degeneracy. PEAC applies to a wide range of cases: coherent implementations like quantum clocks as well as incoherent, stochastic mixtures of components. It allows extracting phase information in setups previously considered unsuitable, for example, when these components spatially overlap. At the same time, it can also be applied in situations where components can be individually resolved, a necessary condition for ellipse fitting. Moreover, PEAC enables phase extraction even when phase fluctuations prevent fringe resolution in correlated interferometer signals (53, 54), providing a valuable toolbox for next-generation platforms (13, 20, 21, 49, 51, 55) for matter-wave sensors with ultracold quantum gases.

2 RESULTS

2.1 Phase Estimation from Amplitude Collapse

To demonstrate its capabilities, we apply PEAC to atom-interferometry-based magnetometry (21–24) in one dimension, a benchmark application well-suited to typical vibration-prone environments and compact devices, even when state-selective interferometry is unavailable. Ultracold ^{87}Rb atoms from a Bose–Einstein condensate (BEC) provide a suitable point source (32) with sub-recoil momentum width, coherence, and access to efficient Bragg diffraction (56). Our experiment (57) creates BECs in a far-detuned crossed optical dipole trap (CDT), typically with 20 000 atoms at 20(5) nK and a condensate fraction exceeding 80 %. When no optical pumping or magnetic quantisation is applied, the atoms occupy a stochastic mixture of all magnetic substates $m_F = \{-1, 0, +1\}$ of the ground-state manifold $|5^2S_{1/2}, F = 1\rangle$. All states are addressed and Bragg-diffracted by a pair of counter-propagating laser beams (58) with a frequency difference $\Delta\omega = 2\pi \times 15.084$ kHz, coupling the two momentum states $|0\hbar k_{\text{eff}}\rangle$ and $|1\hbar k_{\text{eff}}\rangle$ with the modulus $k_{\text{eff}} = 2 \times 2\pi/780.226$ nm of the effective wave vector of the two-photon Bragg transition. With these Bragg pulses, we implement a Mach–Zehnder atom interferometer (MZI) in a $\pi/2$ – π – $\pi/2$ pulse configuration as illustrated in Fig. 1(A). The laser-intensity envelopes of all three pulses are shaped as Blackman window pulses (59, 60) of length $\tau = 100$ μs . We label the temporal separation of the maxima of two consecutive pulses by T . Identical values $T \in [1 \text{ ms}, 3 \text{ ms}]$ result in a total duration of the MZI sequence up to $2T + \tau = 6.1$ ms.

After the MZI, a time of flight (TOF) spatially separates the interferometer output ports associated with the momentum states $|jk_{\text{eff}}\rangle$ for measuring the atom numbers $N_j(\phi) = B_j \pm A_j \cos \phi$ in different momentum classes $j \in \{0, 1\}$, with the interferometric phase ϕ , baseline B_j and amplitude A_j . We define the interferometer signal as the normalised population difference, i. e.

$$S_{\text{all}}(\phi) = \frac{N_0(\phi) - N_1(\phi)}{N_0(\phi) + N_1(\phi)} \cong B_{\text{all}} + A_{\text{all}} \cos \phi, \quad (1)$$

where the signal’s baseline B_{all} and amplitude A_{all} satisfy $|B_{\text{all}}| + |A_{\text{all}}| \leq 1$ and depend on B_j, A_j . For more details on the experimental apparatus and the derivation of S_{all} we refer to Materials & Methods.

By characterising S_{all} , for example by scanning an interferometer fringe, one can extract the interferometric phase ϕ and thus the quantity of interest influencing ϕ . For instance, this could be the projection a_{ext} of an external acceleration in the direction of the Bragg beams. To scan an interference fringe, we offset the phase of the final $\pi/2$ pulse by 20 evenly spaced values of $\phi_{\text{las}} \in [0, 2\pi)$. We perform 15 repetitions per T for improved signal to noise. A typical fringe for $T = 1.6$ ms is shown in the centre panel of Fig. 1(B) by the black trace. We see a clear oscillation and periodicity of the fringe characterised by its amplitude A_{all} , phase ϕ , and baseline B_{all} . If ϕ remains stable between all pulses, a cosine can be fitted to the fringe, providing direct access to these parameters. Conversely, in the absence of phase stability, the amplitude A_{all} and baseline B_{all} of S_{all} can be obtained via a statistical analysis (49, 51, 61, 62), albeit at the cost of losing the phase information. This procedure also can be applied to data obtained under phase-stable conditions, such as our measurements at small T .

To demonstrate this statistical method, we show, at the left margin of Fig. 1(B), a histogram associated with the fringe in black, where the statistics is generated from all 300 contributing measurements. The very left column shows the same histogram converted into a density plot using false-colour coding. We observe the typical double-peak structure of the histogram (49, 61), where the distance of the peaks is roughly given by $2A_{\text{all}}$ and their individual width is determined by baseline fluctuations of B_{all} . This characterisation is valid for a homoscedastic signal, where A_{all} does not fluctuate, as specified in Materials & Methods.

In addition to scanning ϕ via ϕ_{las} for a fixed value of T , we also vary the interferometer time $T \in [1 \text{ ms}, 3 \text{ ms}]$ in steps of $100 \mu\text{s}$. The corresponding histograms are displayed as a composite density plot in Fig. 1(C), where each column is obtained in the same way as in Fig. 1(B) corresponding to the histogram behind the dashed white line at $T = 1.6$ ms. We observe a decrease of the signal amplitude for increasing T with a collapse at $T = 2.1$ ms which is not due to loss of coherence, since A_{all} revives for longer times. This behaviour is caused by an underlying modulation of $A_{\text{all}}(T)$, which is a consequence of the beat of the three signals $S_{m_F}(\phi_{m_F})$ defined in analogy to Eq. (1) and associated with three m_F substates. The m_F substates experience a state-dependent acceleration, in part due to a magnetic field gradient, acquiring different phases ϕ_{m_F} , which induce this characteristic collapse and revival behaviour. The magnetically insensitive $m_F = 0$ substate acquires the phase ϕ_0 , including ϕ_{las} and accelerations and perturbations common to all substates. The magnetically

sensitive states with $m_F \in \{+1, -1\}$ pick up the phases $\phi_{\pm 1} = \phi_0 \pm \theta/2$ with the differential phase

$$\theta \cong 2 k_{\text{eff}} a_{\text{ext}} T^2 (1 + 0.1486 \tau/T) \quad (2)$$

between the two substates, induced by a Zeeman force that accelerates the $m_F = +1$ state by a_{ext} in the direction of the Bragg beams and the $m_F = -1$ state by the same magnitude but in the opposite direction. Here, we correct the conventional MZI phase for finite-pulse durations (63) in τ/T , which can approach 0.1 in our case with $\tau = 100 \mu\text{s}$ for short interferometer times. We present the derivation of the numerical factor in Materials & Methods.

In our experiment, we have additional access to the individual substates by applying the Stern–Gerlach (SG) method (64, 65) during TOF after the MZI: In each momentum exit port we can create a spatial separation of the substates by applying an additional magnetic field gradient as depicted in Fig. 1(A) at right. This method allows us to determine the oscillatory signal S_{m_F} of the individual substates as displayed in the centre panel of Fig. 1(B), along with the corresponding histograms at the right marginals. As expected, we observe the same oscillation amplitude A_{m_F} for all three substates, which is in particular larger than A_{all} . Based on this insight, we conclude that in a non-state-selective setting, the observable is $S_{\text{all}} = \lambda_{+1} S_{+1} + \lambda_0 S_0 + \lambda_{-1} S_{-1}$, where λ_{m_F} are the weights of each substate in the incoherent stochastic mixture.

In the remainder of this section, we focus on this non-state-selective setting. Here, the observable S_{all} can be written as $S_{\text{all}} = B_{\text{all}} + A_{\text{all}} \cos(\phi_0 + \theta_{\text{off}})$. The offset θ_{off} can be interpreted as a geometric phase (52) and depends on θ and λ_{m_F} (cf. Materials & Methods). Here, $B_{\text{all}} = \sum_{m_F} \lambda_{m_F} B_{m_F}$ is the baseline, and

$$A_{\text{all}}(\theta) = A_0 \sqrt{\Delta\lambda^2 \sin^2(\theta/2) + [\lambda_0 + (\lambda_{+1} + \lambda_{-1}) \cos(\theta/2)]^2} \quad (3)$$

is the amplitude, with the population imbalance $\Delta\lambda = \lambda_{+1} - \lambda_{-1}$, assuming $A_{-1} = A_0 = A_{+1}$. In this non-state-selective setting, we cannot access the differential phase θ directly from a histogram recorded for a single interrogation time T , since the weights λ_{m_F} are unknown. However, scanning the interferometric time T allows to infer θ . The underlying reason is the characteristic variation of the amplitude A_{all} with T , as evident from Eqs. (2) and (3), due to the overlay of the three individual interferometer signals with their respective phases.

The resulting method of phase estimation from amplitude collapse (PEAC) is performed by fitting the histogram's probability density function (PDF) for each T to obtain $A_{\text{all}}(T)$, where the form

of the PDF (49, 51, 62) and further details can be found in Materials & Methods. Using $A_{\text{all}}(T)$, we fit Eq. (3) with the help of Eq. (2) to extract the acceleration and further parameters $a_{\text{ext}} = 32.2(1) \text{ mm/s}^2$, $\lambda_0 = 0.42(1)$, $\Delta\lambda = 0.18(1)$, and $A_0 = 0.79(1)$. We calculate the modulated amplitude $A_{\text{all}}(T)$ from these values and plot $\pm A_{\text{all}}(T)$ as black lines in Fig. 1(C). The uncertainty of a_{ext} and all other experimental uncertainties in the following are obtained via bootstrapping (66–68), as explained in Materials & Methods.

Even in the presence of phase instability and a non-state-selective setup, PEAC allows one to estimate the differential phase θ , and thus a_{ext} . We emphasise that no phase can be extracted from a single histogram; however, by considering multiple times T , the collapse of the amplitude A_{all} enables the extraction of the phase. For comparison, as we have direct access to λ_{m_F} from SG population measurements, we directly obtain $\lambda_0 = 0.39(6)$, $\lambda_{-1} = 0.21(3)$, $\lambda_{+1} = 0.40(4)$, $\Delta\lambda = 0.19(5)$, and $A_0 = 0.83(1)$, averaged over all T values. Here, A_0 is the average amplitude of the m_F substates obtained by fitting the individual m_F histograms. These results are in good agreement with those obtained using PEAC. With these values at hand, Eq. (3) can even be applied pointwise. Finally, we highlight that PEAC can even be applied to systems with more than three states, albeit at the cost of a richer beat structure of the amplitude A_{all} (cf. Materials & Methods).

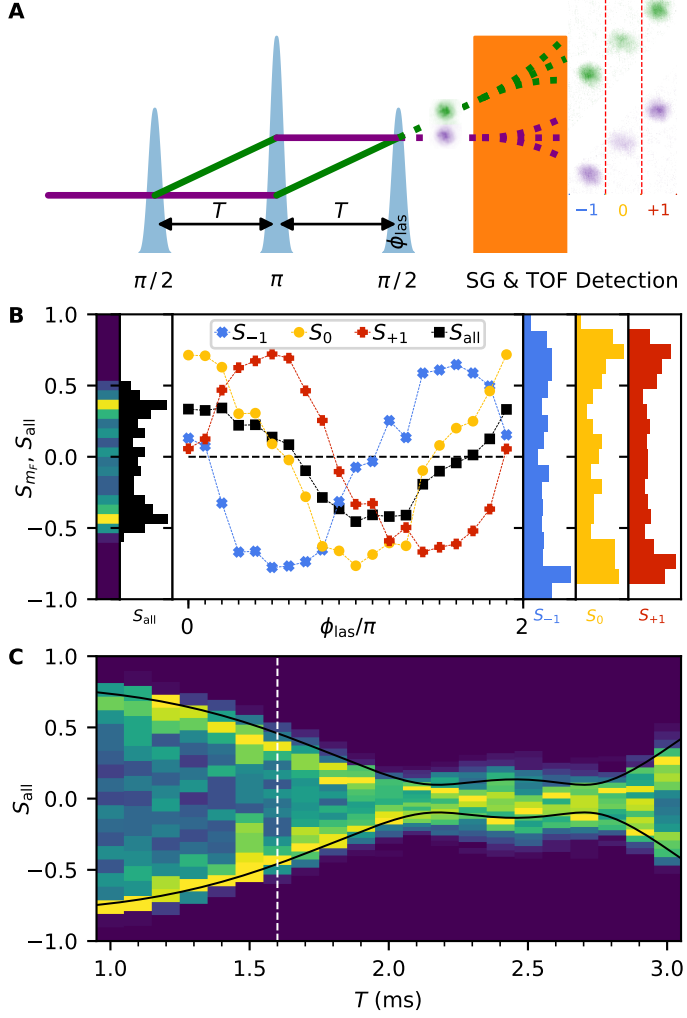


Figure 1: Spacetime diagram and signal extraction. (A) Mach–Zehnder atom interferometer (MZI) realised by three Bragg pulses separated by T , driving transitions between momentum states $|0\hbar k_{\text{eff}}\rangle$ (purple) and $|1\hbar k_{\text{eff}}\rangle$ (green). The phase of the final pulse is shifted by ϕ_{las} , thus scanning the interference fringes at the two exit ports. The MZI is followed by a time of flight (TOF) that spatially separates the exits, during which an optional Stern–Gerlach (SG) field can separate the m_F substates of the $F = 1$ ground state within each momentum class in addition. (B) Fringe scans (20 settings of ϕ_{las} , 15 repetitions averaged, uncertainties omitted for visual clarity) at $T = 1.6$ ms. Without the SG field, we observe the fringe S_{all} (black), with the corresponding histogram from 300 measurements (left marginal, also displayed as a density plot on the far left) has a double-peak structure that depends on the signal’s amplitude. Applying an SG field allows resolving the individual signals S_{m_F} per substate (blue, yellow, red), whose histogram distributions are shown at the right marginal.

[Cap. cont.] The individual signals show equal amplitudes, while the amplitude of S_{all} is reduced due to summation of the individual S_{m_F} with shifted phases. **(C)** The combined density plot of the histograms of S_{all} , obtained for a scan of the interferometer time T , reveals the collapse and revival of the amplitude caused by the incoherent overlay of the three signals S_{m_F} . The black lines trace the calculated amplitude as $\pm A_{\text{all}}$, parametrised by Eq. (3).

2.2 Correlation Measurements – Connection to Ellipse Fitting

As demonstrated in the previous section, PEAC can be used to extract differential phases from the overlay and resulting beat of correlated signals. In addition to emphasising the application to systems without state-selective measurement capabilities, we now shift our focus to correlated systems in a setup allowing for state selection. Acknowledging that correlation measurements also can be carried out in systems with more than two distinct components (41, 69, 70), we restrict our evaluation to a two-state system, similar to typical quantum clocks using $\pi/2$ pulses to generate coherent superpositions between two internal states. We immediately can investigate this in our system by applying the SG method to distinguish the signals S_{m_F} and choosing a symmetric sum of the $m_F = \pm 1$ states while excluding the magnetically insensitive $m_F = 0$ state ($\lambda_0 = 0$). The summed signal

$$S_{\text{sum}} = (S_{-1} + S_{+1})/\sqrt{2}, \quad (4)$$

is scaled by choosing $\lambda_{\pm 1} = 1/\sqrt{2}$, anticipating Eq. (6). Evaluating Eq. (3) for this system gives the amplitude modulation (45, 47)

$$A_{\text{sum}} = \sqrt{2}A_0|\cos(\theta/2)|. \quad (5)$$

In panels (i)–(iv) of Fig. 2(A), we plot the averaged fringes of the individual signals $S_{\pm 1}$ and S_{sum} for four distinct interferometer times $T \in \{1.0 \text{ ms}, 1.4 \text{ ms}, 1.7 \text{ ms}, 2.5 \text{ ms}\}$, i. e. different phases θ . For increasing T , phase noise induces a reduction in the observed fringe amplitudes of S_{+1} and S_{-1} , which are equal in magnitude. The observed fringe amplitude of S_{sum} decreases accordingly, but is in addition modulated by $|\cos(\theta/2)|$ and depends on the phase difference.

In fact, the signals $S_{\pm 1}$ range from being slightly (i) and significantly (ii) out-of-phase, via a vanishing S_{sum} in (iii) for a differential phase $\theta \cong \pi$, to a rephasing at $\theta \cong 3\pi/2$ in (iv). Resorting again to PEAC, we show the corresponding density plot of the histograms in Fig. 2(B), with white

dashed lines marking the chosen times from Fig. 2(A). This visualisation shows clearly the collapse and revival of the amplitude A_{sum} with T and by that with varying differential phase θ . The beat node of the signal at $T = 1.7 \text{ ms}$ ($\theta \cong \pi$) becomes visible, with a secondary node discernible at $T = 3 \text{ ms}$ ($\theta \cong 2\pi$). Fitting the histogram PDF to S_{sum} for each interferometer time T returns the time-dependent amplitude $A_{\text{sum}}(T)$, while fits to $S_{\pm 1}$ can be used to obtain A_0 . The orange line in Fig. 2(B) shows the envelope given by Eq. (5) for averaged values of $A_0 = 0.82(1)$ and $a_{\text{ext}} = 32.2(1) \text{ mm/s}^2$, obtained by bootstrapping the data and fitting. This envelope corresponds to the intrinsic amplitude of the signal, which is larger than the observed fringe amplitude, as the analysis of histograms is robust against phase noise.

Beside fitting the amplitude modulation, a known A_0 allows the pointwise estimation of the differential phase $\theta(T)$ by inverting Eq. (5). To account for the ambiguity of the inverted cosine function, we unwrap the phase. Fitting Eq. (2) to the reconstructed phases returns an external acceleration of $a_{\text{ext}} = 32.2(1) \text{ mm/s}^2$, which is in excellent agreement with our prior results.

We compare PEAC to a more established evaluation scheme for correlated systems based on parametric plots and fitting ellipses (33–35, 71–74). The correlated signals $S_{\pm 1}$ for the interferometer times of Fig. 2(A) are visualised in a bivariate scatter plot in Fig. 2(C), with S_{-1} along the horizontal and S_{+1} along the vertical axis; each measurement realisation is shown as a coloured dot. The colour is chosen to represent the adjusted phase ϕ_{las} , which results in a colour gradient for the performed phase scan as can be seen in sub-figures (i)–(iv). For larger interferometer times $T > 1.6 \text{ ms}$, the colour gradient becomes disordered, showing a transition to the phase-unstable regime of the experiment. While a scan of the phase ϕ_{las} traces the ellipse, the differential phase is encoded in its eccentricity, which can be extracted by fitting an ellipse using the Halíř–Flusser algorithm (72, 73), amongst other methods (21, 33, 75, 76). A detailed explanation of our fitting routine can be found in Materials & Methods. With this approach, we estimate an external acceleration of $a_{\text{ext}} = 31.97(2) \text{ mm/s}^2$, confirming the results obtained by PEAC.

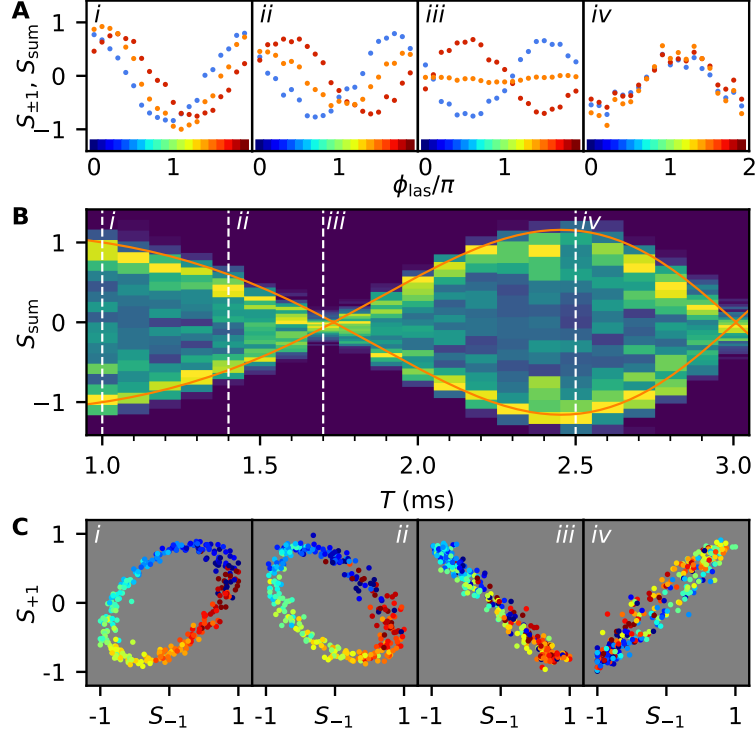


Figure 2: Interference fringes, amplitude collapse, and signal correlation. (A) Coloured dots in panels (i)–(iv) show the averaged interference fringes of S_{+1} (red), S_{-1} (blue), and S_{sum} (orange) for four different values of T , i. e. for distinct differential phases θ . The beat of S_{+1} and S_{-1} leads to a collapsing amplitude of S_{sum} for $\theta \cong \pi$ (iii). Uncertainties are omitted for visual clarity. (B) Collapse and revival of the amplitude A_{sum} (orange) as a function of T , inferred from the underlying histograms of S_{sum} shown as density plot, where brighter regions correspond to higher bin counts. The collapses occur at the beat nodes around $T = 1.7$ ms and $T = 3$ ms. Dashed white lines indicate the times (i)–(iv) from (A). (C) Bivariate scatter plots for times (i)–(iv) of the correlated signals S_{+1} (vertical) and S_{-1} (horizontal), with a colour coding as in (A) indicating the phase scan of ϕ_{las} . The eccentricity of the emerging ellipse encodes the differential phase θ . At $T = 1.7$ ms ($\theta \cong \pi$) and $T = 2.5$ ms ($\theta \cong 3\pi/2$), the ellipses become degenerate and collapse to lines along the anti-diagonal and diagonal, respectively.

In fact, both methods are inherently connected: The principal axes of the ellipses in Fig 2(C) (iii) and (iv) are given by the diagonal and anti-diagonal, see Materials & Methods for more details. The diagonal is proportional to the sum of the bivariate coordinates ($S_{+1} + S_{-1}$) while the anti-diagonal is proportional to their difference ($S_{+1} - S_{-1}$). Rotating the bivariate coordinate system by angle α leads to the definition of the general signal

$$S(\alpha) = S_{-1} \cos \alpha + S_{+1} \sin \alpha. \quad (6)$$

Hence, the special case $S_{\text{sum}} = S(\pi/4)$ denotes the axis along the diagonal and can be accessed even without state-selective measurements for two-component systems. A second case is $S_{\text{diff}} = S(3\pi/4)$, oriented along the anti-diagonal, which can only be inferred in a state-selective setup. Consequently, for two correlated states such as presented here, applying PEAC generalises to performing a statistical histogram analysis of the bivariate data along any angle α . Generally, the rotation angle α encodes the population ratio of the two involved states and reflects any imbalance due to imperfect state preparation. Correspondingly, in Fig. 3 we depict the ellipses aligned to their principal axes S_{sum} and S_{diff} , i. e. rotated by $\pi/4$ clockwise, for $T = 1.7$ ms (left) and $T = 2.5$ ms (right) in the bivariate variables ($S_{\text{sum}}, S_{\text{diff}}$) with complementing histograms at the marginals. The displayed

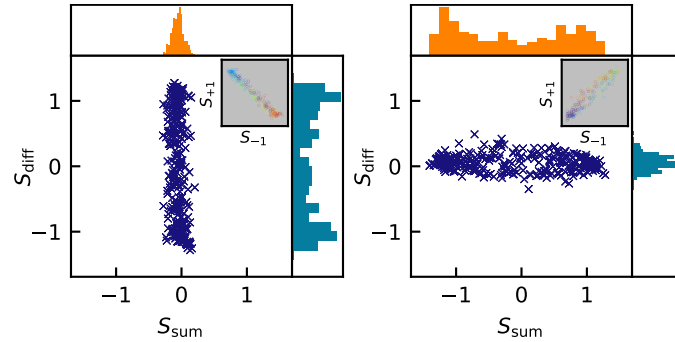


Figure 3: Rotated bivariate scatter plots and histograms. Rotating the original correlation signals (insets) for $T = 1.7$ ms ($\theta \approx \pi$, left) and $T = 2.5$ ms ($\theta \approx 3\pi/2$, right) by $\pi/4$ clockwise aligns the ellipses to their principal axes, which correspond to S_{sum} (horizontal) and S_{diff} (vertical). The marginal distributions show the histograms of S_{sum} and S_{diff} , illustrating that the two exchange their roles at the respective degeneracy points of θ . This representation visualises the intrinsic link between ellipse-based estimation based on bivariate fitting and PEAC applied to S_{sum} and S_{diff} . Note that S_{diff} is only accessible by state-selective detection.

ellipses are close to degeneracy, i. e. $\theta \cong \pi$ (left) and $\theta \cong 2\pi$ (right), where the method of ellipse fitting has known limitations. Especially large baseline fluctuations lead to large biases of the estimated phase close to these degeneracy points. In the following section, we investigate this systematic error and compare PEAC in trueness and precision to the ellipse fitting approach.

2.3 PEAC Performance

To quantify the performance of PEAC, we assess the trueness and precision of phase estimation. Figure 4(A) displays the unwrapped phase θ_{rec} , reconstructed individually from the experimental data for each T from algebraic ellipse fitting (dark blue crosses, masked by orange crosses for most data points) using the Halíř and Flusser algorithm (72, 73) (see Materials & Methods for details). For a complementary theoretical analysis establishing a connection between experiment and theory, we use the control variable θ_{set} , which we convert to the corresponding T via Eq. (2) using $a_{\text{ext}} = 32.2(1) \text{ mm/s}^2$. Ideally, we expect the black dashed line representing identity, corresponding to perfect phase reconstruction $\theta_{\text{rec}} = \theta_{\text{set}}$, yet notable deviations of the experimental data occur. This discrepancy becomes more evident for the numerical replication of the experiment, shown as the dark blue line. We use the experimentally inferred parameters characterising the signals (see details in Materials & Methods). In essence, the numerical replication allows for a much finer sampling of θ_{set} . The largest discrepancies occur at $\theta_{\text{set}} = \pi\mathbb{Z}$, i. e. at points of degeneracy, which are a fundamental limitation to ellipse-based phase estimation (33, 74). We experimentally study one of these degeneracy points in more detail: The inset at $\theta_{\text{set}} = \pi$ illustrates this discrepancy through a finer experimental sampling in T . In this inset, the centre of each rectangle denotes the mean, while its height is twice the empirical standard deviation extracted from bootstrapping, caused by the statistical nature of the baseline fluctuations. The experimental data obtained from ellipse fitting (dark blue) exhibits the same qualitative behaviour as the numerical replication, thereby confirming the validity of our theoretical model. Hence, a bias $\theta_{\text{bias}} = \theta_{\text{rec}} - \theta_{\text{set}}$ in the vicinity of the degeneracy points deteriorates the trueness of the estimated phase.

Figure 4(B) presents the amplitudes A_{sum} (orange) and A_{diff} (blue) of S_{sum} and S_{diff} , extracted from histogram fits. The data clearly underline the collapse and revival behaviour. As in panel (A), we present the ideal amplitudes $A_{\text{sum}} = \sqrt{2}A_0|\cos(\theta_{\text{set}}/2)|$ and $A_{\text{diff}} = \sqrt{2}A_0|\sin(\theta_{\text{set}}/2)|$ by black

dashed lines. Fits to the numerical replication lead to the solid lines for A_{sum} (orange) and A_{diff} (blue), which are phase shifted by π , as expected from Fig. 3. The insets magnify the deviation near the degeneracy points. Applying PEAC to the experimental data, we infer $\theta_{\text{rec}}(T)$ via Eq. (5) and thus obtain the orange crosses in panel (A) and rectangles in its inset. See Materials & Methods for a detailed description of the full protocol. Compared to the reconstruction via the ellipse method, we see a larger standard deviation, and by that a decrease in precision. However, the bias is reduced as can be seen in the inset of panel (A), increasing the trueness and the overall accuracy.

The numerical replication allows us to quantify the respective bias θ_{bias} of the different estimation methods, shown in Fig. 4(C) as solid lines (dark blue: ellipse, orange: S_{sum} , blue: S_{diff}). Enabled by state-selective detection through the SG method and post-processing of the data, the difference signal S_{diff} is also analysed using PEAC, revealing that the bias is π -phase shifted relative to S_{sum} . The traces directly show the averaged bias and are a measure of trueness (high if $\theta_{\text{bias}} \approx 0$), while the shaded areas represent the uncertainty $\pm\Delta\theta$ in phase reconstruction, obtained from statistical repetitions as detailed in Materials & Methods, and quantify the precision: smaller uncertainty bands correspond to higher precision. This plot illustrates the challenges of the ellipse fitting method: While it can achieve high precision, it suffers from major bias leading to low trueness, particularly at points of degeneracy. In fact, the ellipse fitting method is unbiased only in the circular case, i. e. odd multiples of $\theta = \pi/2$. In contrast, PEAC substantially reduces the bias across all phases and therefore enhances the trueness at the expense of precision. We also observe that S_{sum} and S_{diff} reverse their roles at opposing degeneracy points, such that applying PEAC to S_{sum} around $\theta \approx \pi$ benefits from higher precision, while analysing S_{diff} is favourable around $\theta \approx 2\pi$. Considering the bivariate ($S_{\text{sum}}, S_{\text{diff}}$) plane of Fig. 3, we understand this behaviour geometrically: The bias and precision are only substantially reduced when the histogram is obtained by projecting along the minor axis of the ellipse. We give more insights into the bias' origin in Materials & Methods. Along the favourable minor axis, PEAC reduces the bias at critical points by roughly 80 % compared to ellipse fitting. Even along the major axis, we observe a reduction of 50 %, although with a high uncertainty, which depends on the number of measuring points and further optimisation schemes (51). Thus, PEAC achieves higher trueness compared to the ellipse method, which is a necessary condition for high-accuracy measurements, for which both trueness and precision are essential.

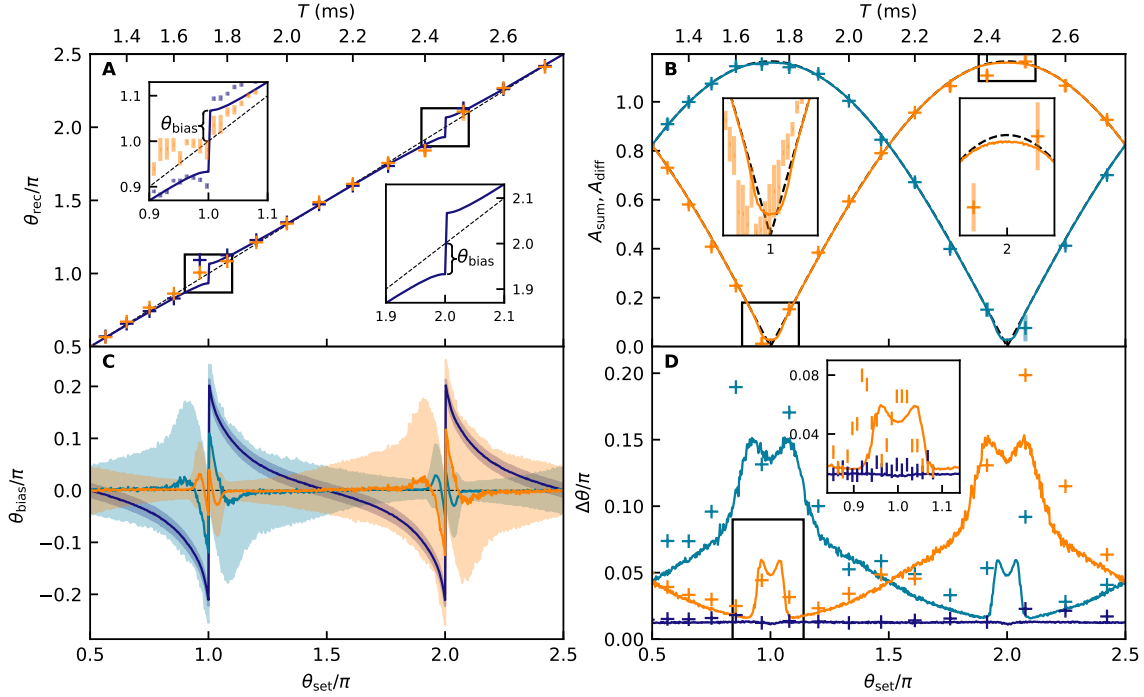


Figure 4: Performance of phase estimation: Ellipse fitting versus PEAC. Comparison of ellipse fitting (dark blue) and PEAC along the S_{sum} (orange) and S_{diff} (light blue) directions. Experimental data are shown as crosses (error bars omitted for clarity) or rectangular bars, with centres indicating the mean and heights equal to twice the bootstrapped standard deviation. Solid lines are values obtained from numerical replications of the experiment. The dashed lines correspond to the set phases and amplitudes as reference values free of fitting errors. We convert the set phase θ_{set} via Eq. (2) to T . **(A)** Reconstructed phase. The inset shows that ellipse fitting leads to a large bias $\theta_{\text{bias}} = \theta_{\text{rec}} - \theta_{\text{set}}$ near degeneracy, despite high precision, while PEAC along the minor axis S_{sum} exhibits larger uncertainty but a reduced bias. **(B)** Modulation of the amplitudes A_{sum} and A_{diff} obtained from histogram fits along the two principal axes. We observe a deviation at degeneracy, contributing to PEAC's remaining bias. **(C)** Bias obtained from numerical replications. PEAC along the favourable (minor) axis reduces the bias by 80 %, substantially enhancing trueness. The semi-transparent bands give the uncertainties extracted from 1000 replicated experiments. **(D)** Precision of phase estimation. Ellipse fitting maintains low uncertainty across all θ_{set} , while PEAC of S_{sum} achieves comparable precision only near, but not at the degeneracy point $\theta_{\text{set}} = \pi$, as would be expected from simple Gaussian uncertainty propagation. This behaviour arises from an ambiguity in the histogram's PDF for small amplitudes.

Finally, we compare the precision of both methods by investigating the phase uncertainty $\Delta\theta$ shown as the height of the shaded areas of panel (C). The values of the uncertainty are displayed as solid lines in Fig. 4(D) for a direct comparison. To benchmark the theoretical analysis, we also add the corresponding experimental values as crosses and vertical bars in the inset around degeneracy (dark blue: ellipse fitting, orange: S_{sum} , blue: S_{diff}). The uncertainty of the ellipse method is almost constant across all phases and consistently lower than that of PEAC, for both S_{sum} and S_{diff} . Nevertheless, PEAC can achieve uncertainty levels as low as ellipse fitting for specific phases near, but not exactly at degeneracy. In quantum clock interferometry, simple Gaussian uncertainty propagation suggests $\Delta\theta = \Delta A_{\text{sum}} / |\partial_\theta A_{\text{sum}}|$, where ΔA_{sum} is the uncertainty of the oscillation amplitude. Following this intuition, the amplitude $A_{\text{sum}} = \sqrt{2}A_0|\cos(\theta/2)|$ exhibits its steepest slope and by that the lowest uncertainty at $\theta = \pi$. In contrast, a vanishing slope at $\theta = 2\pi$ implies a diverging phase uncertainty and explains why the major axis is unfavourable for PEAC along S_{sum} . However, as shown in the inset of Fig. 4(B), we observe that near the degeneracy point $\theta_{\text{set}} \cong \pi$, the fitted value of A_{sum} deviates from the expected behaviour. This deviation and the connected increase in uncertainty arise from a merging of the two maxima of the PDF for low amplitudes, resulting in a single-peak PDF. Although no closed analytical expression describes this transition, a numerical analysis reveals that it occurs when $A/\sigma < 1.78$, where σ is the standard deviation of the baseline fluctuations. For phases that result in lower amplitudes than this threshold, we observe an increase of the phase uncertainty $\Delta\theta$, which is a consequence of ambiguities in the fit parameters A_{sum} and σ . Therefore, despite the expectation from Gaussian uncertainty propagation, the minimal phase uncertainty is not observed at the degeneracy point $\theta_{\text{set}} = \pi$, i. e. at vanishing signal amplitude, contradicting the common belief in quantum clock interferometry (52). In fact, minimal uncertainty is reached near, but not at the aforementioned degeneracy point, namely where the signal amplitude is small but still finite. At this point, the level of uncertainty is similar to that of ellipse fitting, but the trueness is superior.

3 DISCUSSION

Although the statistical analysis of the noisy signal of an interferometer, such as histogram-based estimation of the underlying probability density function (PDF), provides access to the oscillation amplitude and baseline fluctuations, it inherently lacks phase information. When two such signals are correlated, common-mode noise is suppressed, allowing for the extraction of a differential phase θ from the bivariate data, for example from fitting to ellipses (33–35, 71–74) or Lissajous curves (17, 77).

In this work, we establish a geometric connection between these two paradigms: We introduce phase estimation from amplitude collapse (PEAC), a method that performs a statistical analysis along a suitably chosen projection direction in the bivariate plane. It extracts a differential phase from the observed amplitude, which shows a characteristic collapse and revival due to the beat of overlaying signals. Unlike conventional ellipse fitting, which becomes ill-posed near degeneracy points ($\theta = \pi\mathbb{Z}$) where the ellipse collapses to a noisy line (74), PEAC always fits the correct PDF of the marginal distribution. This procedure eliminates the issues of a geometric degeneracy and reduces systematic bias, thereby enhancing trueness and overall accuracy. We highlight five key advancements:

- (i) PEAC allows extracting differential phases in setups where the individual signals cannot be resolved independently, for example in non-state-selective setups where the individual components overlap spatially, overcoming one limitation of conventional ellipse fitting.
- (ii) It is a complementary analysis applicable to any system employing ellipse fitting without the need for additional experimental resources. While it generally requires more data points than ellipse fitting due to its statistical nature, PEAC becomes a powerful tool when sufficient statistics are available. It generalises naturally by projecting along an angle α in the bivariate plane, enabling phase estimation of arbitrary mixtures of the correlated signals. Even more, PEAC improves the trueness of the estimated phase by reducing the bias and systematic error near degeneracy. This enhancement is not merely a technical improvement, but critical for high-accuracy null measurements, for example envisioned for tests of fundamental physics (7–10).
- (iii) We demonstrate that PEAC directly connects to quantum clock interferometry (39–44) and answers the question of optimal performance, which in fact is close to, but not exactly at degeneracy.

Notably, we observe no divergence of phase sensitivity at degeneracy, as predicted from geometric phase amplification (52) when neglecting the vanishing oscillation amplitude.

(iv) Beyond two correlated signals, we demonstrate the applicability of PEAC to three correlated signals, without requiring to resolve them individually. The technique is therefore established as a complementary analysis of three- or higher-dimensional ellipse methods (69). Moreover, it can be applied to scenarios where an amplitude modulation is introduced deliberately into only one signal, situations that are inaccessible to ellipse fitting. For example, it extends contrast-envelope fits (78–80), a standard technique for atom interferometry, where the interferometer is partially or dynamically opened to control the visibility of the interference pattern, or applies to schemes where a phase modulation translates into a characteristic amplitude modulation (81).

(v) Finally, PEAC is broadly applicable to a wide range of setups, from fully phase-stable to noisy, non-phase-stable regimes. The sensitivity of phase estimation can be enhanced by resorting to higher-order atom diffraction, demonstrating that it scales with increasing momentum transfer, and can be applied to periodic signals beyond atom interferometry, such as atomic clocks (53, 54) or optical interferometers.

PEAC can be further improved, for example by integrating it with other statistical inference techniques such Bayesian methods (17, 51, 82) or maximum likelihood estimation (83), moving beyond the least-square fitting of PDFs used in this work. As these techniques pose a more targeted approach to parameter estimation, we anticipate a further reduction of the bias. Similarly, PEAC can be combined with recent developments in ellipse fitting, such as geometric procedures that minimise the bias with the help of optimised cost functions (21). Using PEAC in combination with ellipse fitting and inducing a feedback loop between these procedures can help to decrease the bias in a joint phase estimation protocol, especially close to degeneracy. One could further allow for adaptive bin sizes within a single histogram and automatically assess the number of required bins to resolve the important features of the PDF without increasing the statistics. Such a procedure would also lead to improved initial guesses for the fitting routines. While PEAC is a classical statistical method, combining it with quantum input states, such as optimally squeezed states (84), has the potential to surpass current limits in quantum metrology and to advance perspectives in a broad range of applications.

4 MATERIALS AND METHODS

4.1 Experimental System and Measurements

Our experimental setup produces BECs in a crossed optical dipole trap (CDT) by forced evaporative cooling (57, 85). To perform measurements in free space, the atoms are released from the CDT into free fall. Prior to the start of the MZI sequence, an expansion time of 3 ms allows for the conversion of the mean-field to kinetic energy. After this expansion, the momentum spread of the ensemble is typically (58) $\Delta p = 0.13(3) \hbar k_{\text{eff}}$. The laser beams used for Bragg diffraction are superimposed onto one of the CDT beams in a counter-propagating setup, oriented perpendicular to gravity and the free-fall of the ensembles. This ensures an initial momentum of $p_0 = 0$ in the direction of Bragg diffraction. To drive two-photon transitions, the Bragg beams are detuned by $\Delta = 2\pi \times 3.2$ GHz from the excited state manifold $|e\rangle = |5^2P_{3/2}, F = 2\rangle$, transferring momentum $\hbar k_{\text{eff}} = \hbar 2 \times 2\pi/780.226$ nm along the Bragg axis. In this article we rely on first-order Bragg diffraction by choosing a detuning $\Delta\omega = 2\pi \times 15$ kHz between the two beams, while our setup also allows for higher-order diffraction (58) by adjusting $\Delta\omega$ to other resonances. A Blackman window $f(t) = 0.42 - 0.5 \cos(2\pi t/\tau) + 0.08 \cos(4\pi t/\tau)$ for $0 \leq t \leq \tau$ as a smooth pulse shape ensures efficient transfer between the coupled momentum states and reduces the population of parasitic momenta. We use a pulse length of $\tau = 100$ μ s as a compromise between velocity selectivity and diffraction efficiency, adjusting the peak Rabi frequency of the pulse to adapt for the $\pi/2$ and π pulses. Following each MZI, a time of flight (TOF) of typically 15 ms–30 ms is applied to separate the two interferometer ports spatially for detection. We perform resonant absorption imaging (86) of the atomic densities to gain access to the atom numbers $N_{0/1}$ in each of the interferometer ports. Without optical pumping or a state-selective SG measurement, the densities of the three m_F substates will spatially overlap and cannot be distinguished. However, our setup also allows using the SG method, by applying a magnetic field gradient after the MZI, generated by one of the magnetic coils used for the magneto-optical trap, separating the m_F substates spatially via the Zeeman force. A time delay of 1 ms between the second $\pi/2$ pulse and the introduction of the magnetic field gradient prevents spurious phase contributions to the interferometer phase. The applied weak gradient is left on for a total of 24 ms until detection to ensure proper state separation.

4.2 Derivation of Signal S

The normalised difference between the atom numbers $N_{0/1}(\phi) = B_{0/1} \pm A_{0/1} \cos \phi$ detected in the two momentum classes leads to the signal

$$S = \frac{N_0 - N_1}{N_0 + N_1} = \frac{\Delta B + 2\bar{A} \cos \phi}{2\bar{B} + \Delta A \cos \phi}, \quad (7)$$

introducing the mean and differential baseline $\bar{B} = (B_0 + B_1)/2$ and $\Delta B = B_0 - B_1$, as well as the mean and differential amplitude $\bar{A} = (A_0 + A_1)/2$ and $\Delta A = A_0 - A_1$, respectively. Having only two exit ports, the total atom number $N_0 + N_1$ must be preserved and must be independent of the interferometric phase ϕ , implying $A_1 = A_0$. As a result, we find

$$S = \frac{\Delta B}{2\bar{B}} + \frac{A_0}{\bar{B}} \cos \phi. \quad (8)$$

In general, A_j, B_j are suitable random variables describing experimental stochastic fluctuations of baselines and amplitudes, which may cause a heteroscedastic signal.

It is typically assumed that the baseline noise $\Delta B/(2\bar{B})$ is normally distributed and dominant, such that A_0/\bar{B} can be treated as constant (51). Observing a homoscedastic signal, i. e. in our setting treating A_0/\bar{B} as constant, is possible if both random variables are correlated. Assuming that A_0 and \bar{B} are perfectly correlated gives

$$A_0 = \sqrt{\frac{\mathbb{V}[A_0]}{\mathbb{V}[\bar{B}]}} (\bar{B} - \mathbb{E}[\bar{B}]) + \mathbb{E}[A_0], \quad (9)$$

where $\mathbb{E}[\cdot]$ denotes the expectation value and $\mathbb{V}[\cdot]$ the variance of a random variable. To have constant A_0/\bar{B} and excluding the trivial constant signal, i. e. $\mathbb{E}[A_0] = 0$, the condition

$$\frac{\mathbb{E}[A_0]}{\mathbb{E}[\bar{B}]} = \sqrt{\frac{\mathbb{V}[A_0]}{\mathbb{V}[\bar{B}]}} \quad (10)$$

must be satisfied. With Eq. (10), we observe from the condition of perfect correlation (9) that the signal takes the form

$$S = \frac{\Delta B}{2\bar{B}} + \frac{\mathbb{E}[A_0]}{\mathbb{E}[\bar{B}]} \cos \phi, \quad (11)$$

in which only $\Delta B/(2\bar{B})$ fluctuates.

Assuming normally distributed baselines $B_j \sim \mathcal{N}(\mu_j, \sigma_j^2)$ with mean μ_j and standard deviation σ_j , the fluctuations must be sufficiently small to resolve a signal, i. e. $\mu_j \gg \sigma_j$. If we additionally

assume the same baseline fluctuations in both exits of the interferometer, i.e. $\sigma_1 = \sigma_2$, we can treat the mean baseline as constant $\bar{B} \sim \mathcal{N}(\bar{\mu}, \sigma_1^2/2) \cong \bar{\mu} = \mathbb{E}[\bar{B}]$ with $\bar{\mu} = (\mu_1 + \mu_2)/2$ and $\sigma_1 = \sigma_2 \ll \bar{\mu}$. With these stipulations we finally arrive at a homoscedastic signal

$$S = B + A \cos \phi, \quad (12)$$

with $B = \Delta B/(2\mathbb{E}[\bar{B}]) \sim \mathcal{N}(\mu, \sigma^2)$ of mean $\mu = (\mu_1 - \mu_2)/(2\bar{\mu})$ and variance $\sigma^2 = \sigma_1^2/(2\bar{\mu}^2)$, that has no amplitude fluctuations and only normally distributed baseline fluctuations.

4.3 Finite-Pulse Duration

The finite duration τ of the Bragg pulses can be a significant fraction of the interrogation time T , ranging from 3 % up to 10 % in our experiments, and therefore introduces a non-negligible phase contribution (63, 87–89) that must be included in our phase analysis. To incorporate this phase contribution, we resort to a numerical treatment, necessary for time-dependent pulses, and define the accumulated time-dependent pulse area

$$\phi_1(t) = \int_0^t dt' \Omega(t') \quad (13)$$

with the time-dependent Rabi frequency train $\Omega(t) = \Omega_0[f(t) + 2f(t-T) + f(t-2T)]$ described by the Blackman envelope f . As in the experiment, we choose $0.42 \Omega_0 \tau = \pi/2$ accounting for the $\pi/2$ pulses at $t = 0$ and $t = 2T$ as well as for the π pulse at $t = T$. An external acceleration a_{eff} induces a time-dependent Doppler detuning $k_{\text{eff}}a_{\text{eff}}t$, assuming the atoms are initially on resonance in agreement with our experimental realisation. For example, to obtain the phase of the $m_F = +1$ state induced by a_{eff} we evaluate (63)

$$\theta(T)/2 = \int_0^{2T+\tau} dt k_{\text{eff}}a_{\text{ext}}t \sin[\phi_1(t)] \quad (14)$$

numerically for $\tau = 100 \mu\text{s}$ and various $T \in [1 \text{ ms}, 3 \text{ ms}]$. For a simplified analytical expression, we fit $\theta(T) = 2k_{\text{eff}}a_{\text{eff}}T^2(1 + \gamma\tau/T)$ to the resulting values and obtain the fit parameter $\gamma \cong 0.1486$.

4.4 General Amplitude Modulation

Here, we present the derivation of the amplitude modulation A_{all} in Eq. (3) of the main text. A sum of n cosines weighted by $\lambda_i \in \mathbb{R}$ with a common phase ϕ_0 , but possible different phases θ_i , results (90) in

$$\sum_{i=1}^n \lambda_i \cos(\phi_0 + \theta_i) = A[\{\lambda_i\}, \{\theta_i\}] \cos(\phi_0 + \theta_{\text{off}}) \quad (15a)$$

with the modulated amplitude

$$A^2 = \sum_{i=1}^n \lambda_i^2 + 2 \sum_{i=1}^n \sum_{j>i}^n \lambda_i \lambda_j \cos(\theta_i - \theta_j) \quad (15b)$$

and offset phase

$$\tan \theta_{\text{off}} = \frac{\sum_{i=1}^n \lambda_i \sin \theta_i}{\sum_{i=1}^n \lambda_i \cos \theta_i}. \quad (15c)$$

In our setting we have $\{\lambda_i\} = \{\lambda_{m_F}\}$, $\theta_0 = 0$, and $\theta_{\pm 1} = \pm \theta/2$, such that after algebraic manipulations we obtain Eq. (3) of the main text and find for the offset phase

$$\tan \theta_{\text{off}} = \frac{\lambda_0 + \Delta \lambda \sin(\theta/2)}{\lambda_0 + (\lambda_{-1} + \lambda_{+1}) \cos(\theta/2)}. \quad (16)$$

A point-wise phase reconstruction is possible if all λ_{m_F} are known and can be obtained from

$$\cos(\theta/2) = \frac{\lambda_0(\Lambda - \lambda_0)}{\Delta \lambda^2 - (\Lambda - \lambda_0)^2} \pm \sqrt{\frac{\Delta \lambda^2 [\Delta \lambda^2 + 2\Lambda \lambda_0 - \Lambda^2]}{[\Delta \lambda^2 - (\Lambda - \lambda_0)^2]^2} - \frac{(A_{\text{all}}/A_0)^2}{\Delta \lambda^2 - (\Lambda - \lambda_0)^2}}, \quad (17)$$

where we introduced $\Lambda = \sum_{m_F} \lambda_{m_F}$.

4.5 Histogram Fitting Routine

We generate all histograms by binning the 300 measuring points of each signal into $\sqrt{300} \cong 18$ bins. The width of the bins for each T setting is adapted so that all 18 bins are cover the whole range of acquired data and therefore depends on the signal's maximum value. This change of bin size can be seen in Figs. 2(B) and 3. The square root rule is an established rule for creating histograms with an adequate resolution in our setting, although we note that this is not a trivial matter and leaves plenty of room for refinement (91, 92).

4.5.1 Probability Density Function

We start from the signal form of the main text, i. e. $S = B + A \cos(\phi_0 + \theta_{\text{off}})$, where A is a constant amplitude, ϕ_0 is a (potentially fluctuating) phase that is used to scan a fringe, θ_{off} is a fixed phase, and B is a normally distributed random variable describing baseline fluctuations. We use a linear scan with a fine step size to scan ϕ_0 in our experiment, such that even in the phase-stable setting using a uniform phase distribution with support $[0, 2\pi]$ is a good approximation, which (ironically) improves if phase fluctuations are relevant. Otherwise, one has to adapt for the underlying PDF of the phase scan. Consequently, the resulting PDF of the amplitude is (93)

$$f_A(a) = \begin{cases} 1/\left(\pi\sqrt{A^2 - a^2}\right), & -A < a < A \\ 0, & \text{else} \end{cases}. \quad (18)$$

Moreover, we assume that baseline fluctuations are independent and identically distributed, such that their PDF is given by a normal distribution

$$f_B(b) = \frac{1}{\sigma\sqrt{2\pi}} \exp\left[-\frac{(b - \mu)^2}{2\sigma^2}\right], \quad (19)$$

with mean μ and variance σ^2 , according to the central limit theorem. The PDF of a sum of two random variables is the convolution $*$ of their respective PDFs, i. e. the PDF of the signal S is

$$f_S(\beta) = (f_A * f_B)(\beta) = \frac{1}{\sigma\sqrt{2\pi^3}} \int_{-A}^A da \frac{1}{\sqrt{A^2 - a^2}} \exp\left[-\frac{(\beta - a - \mu)^2}{2\sigma^2}\right]. \quad (20)$$

For $A > \sigma$, this PDF shows a symmetric double-peak distribution. These maxima are roughly separated by $2A$, their width is determined by σ , and the PDF rapidly decays for $|\beta| \rightarrow \infty$. Contrary, for $A < \sigma$ the two maxima start to overlap, causing the double-peak structure to become washed out.

4.5.2 Initial Guesses

For fitting the histogram's PDF, cf. Eq. (20), we use `scipy.optimize.curve_fit` from the `scipy` package in `python` (94), returning A_{fit} , σ_{fit} , and μ_{fit} . To guarantee reliable convergence of the fit, accurate initial parameter guesses are essential. *Nota bene*: The `scipy.optimize.curve_fit` method is based on a gradient approach which is computationally efficient, however, the PDF f_S is

not differentiable with respect to A even in a distributional sense. We noticed issues related to this non-differentiability when using poor initial guesses.

The initial guess of the histogram's mean μ_{guess} is given by explicitly calculating the signal's mean. A reliable initial guess for the standard deviation of the baseline fluctuations σ_{guess} can be extracted from the rapid decay $|\beta| \rightarrow \infty$ of the PDF: First, we determine one maximum of the histogram at β_{\max} . Starting from this maximum, we scan outward across the histogram to locate the position $\beta_k = k\beta_{\max}$ with $0 < k < 1$, where the maximum has dropped to the fraction k . We then roughly approximate the rapid outward drop of the histogram by an exponential decay, resulting in

$$\sigma_{\text{guess}} = |\beta_{\max} - \beta_k| \sqrt{-1/(2 \ln k)}, \quad (21)$$

which is well-defined since $\ln k < 0$. The choice $k = 1/4$ gave robust and reliable initial guesses.

The initial guess of the amplitude A_{guess} is obtained from the above guesses via

$$A_{\text{guess}} = |\beta_{\max} - \mu_{\text{guess}}| + \sigma_{\text{guess}}. \quad (22)$$

We numerically confirmed that $\beta_{\max} \cong \mu \pm (A - \sigma)$, up to numerical factors. An analytical form is only possible for $\sigma = 0$, where we find $\beta_{\max} = \mu \pm A$ as expected.

4.5.3 Fitting Procedure

When fitting a single histogram we make use of the initial guesses according to Sect. 4.5.2.

In the state-selective case, we have access to $S_{\pm 1}$, S_{sum} , and S_{diff} , such that we can perform four histogram fits. We start by fitting the histogram's PDF to $S_{\pm 1}$ based on the initial guesses from the previous section, returning $A_{\pm 1, \text{fit}}$, $\sigma_{\pm 1, \text{fit}}$, and $\mu_{\pm 1, \text{fit}}$. We set A_0 to be the mean $(A_{+1, \text{fit}} + A_{-1, \text{fit}})/2$. Next, we use the mean $(\sigma_{+1, \text{fit}} + \sigma_{-1, \text{fit}})/2$ as the initial guess for $\sigma_{\text{sum, fit}}$ and $\sigma_{\text{diff, fit}}$, unless it is smaller than any bin width of $S_{\pm 1}$. In the latter case, we use the initial guess routine of Sect. 4.5.2 for $\sigma_{\text{sum, fit}}$ and $\sigma_{\text{diff, fit}}$. Both S_{sum} and S_{diff} fluctuate with the same standard deviation σ , identical to that of $S_{\pm 1}$, because for $B_i \sim \mathcal{N}(\mu_i, \sigma_i^2)$ the random variable $Z = \lambda_1 B_1 + \lambda_2 B_2$ is also normally distributed, i. e. $Z \sim \mathcal{N}(\lambda_1 \mu_1 + \lambda_2 \mu_2, \lambda_1^2 \sigma_1^2 + \lambda_2^2 \sigma_2^2)$. Since we have $\sigma_{1,2} = \sigma$ and $\lambda_{\pm 1} = 1/\sqrt{2}$, we find $\lambda_1^2 \sigma_1^2 + \lambda_2^2 \sigma_2^2 = \sigma^2$.

Finally, we restrict the parameter $A_{\text{sum, fit}}$ to $[0, \sqrt{2}A_0, \text{fit}]$, but otherwise estimate the amplitudes as in Sect. 4.5.2. These limits ensure the correct connection between $S_{\pm 1}$ and S_{sum} , allowing for a phase reconstruction via Eq. (5).

We apply the same procedure to the difference signal, but use $S_{\text{diff}} = \sqrt{2}A_0|\sin(\theta/2)|$ for phase reconstruction. Unlike the amplitude and standard deviation of the baseline fluctuations, the mean is not an issue. Therefore, we use the mean of the respective signal as the initial guess.

4.6 Ellipse and Fitting Routine

As a comparison to PEAC, we deploy an established approach to evaluate correlated signals based on fitting an ellipse to a bivariate parametric plot of two signals. We assume that the signals of the $m_F = \pm 1$ substates have the parametric form $S_{\pm 1}(\phi_0) = B_{\pm 1} + A_{\pm 1} \cos(\phi_0 \pm \theta/2)$ with amplitudes A_i , baselines B_i , common phase ϕ_0 , and differential phase θ . The bivariate data span ellipses in the (S_{+1}, S_{-1}) plane, where the eccentricity of the ellipse encodes the differential phase. We translate the parametric form into the algebraic description $0 = c_{+1}^2 S_{+1}^2 + c_{-1}^2 S_{-1}^2 + c_0 S_{+1} S_{-1} + d_{+1,-1} S_{+1} + d_{-1,+1} S_{-1} + d_0$ of conic sections with the coefficients

$$\begin{aligned} c_i &= (A_i \sin \theta)^{-1} & \text{and} & \quad c_0 = -2c_{+1}c_{-1} \cos \theta \\ d_{i,j} &= -2B_i c_i^2 - B_j c_0 & \text{and} & \quad d_0 = B_{+1}^2 c_{+1}^2 + B_{-1}^2 c_{-1}^2 + B_{+1} B_{-1} c_0 - 1 \end{aligned} \quad (23)$$

which for ellipses have to satisfy $c_0^2 - 4c_{+1}^2 c_{-1}^2 = -4c_{+1}^2 c_{-1}^2 \sin^2 \theta < 0$ for $\theta \in (0, \pi) + \pi\mathbb{Z}$. For $\theta = \pi\mathbb{Z}$ the ellipse degenerates onto straight lines in the case of perfect (anti-)correlation. Direct evaluation of Eq. (23) gives access to the differential phase

$$\theta = \pm \arccos \left(-c_0 / \sqrt{4c_{+1}^2 c_{-1}^2} \right) + \pi\mathbb{Z}. \quad (24)$$

To extract the experimental differential phase as a benchmark for PEAC, we use the Halíř and Flusser algorithm to fit the algebraic ellipse equation to our data (72, 73). Since the algebraic description can be scaled by any constant, we ensure positivity of the fit parameters c_{+1}^2 and c_{-1}^2 , fixing the sign of c_0 , which is important when evaluating Eq. (24).

As mentioned in the main text, diagonalising the quadratic form $c_{+1}^2 S_{+1}^2 + c_0 S_{+1} S_{-1} + c_{-1}^2 S_{-1}^2$ and assuming equal amplitudes $A_{+1} = A_{-1}$ implying $c_{+1} = c_{-1}$ leads to the two principal axes of the ellipse along the $(1, \text{sgn}(c_0))^T / \sqrt{2}$ and $(1, -\text{sgn}(c_0))^T / \sqrt{2}$ direction of the bivariate coordinate space, i. e. the diagonal and anti-diagonal depending on the sign of c_0 .

4.7 Bootstrapping

We assume that the experimental uncertainties of the homoscedastic interferometric signals S stem from fluctuations of the signal's baseline B , parametrised by the standard deviation σ of a normal distribution in our model, while the amplitude of the signal is assumed to be constant. Since for any interferometer time T we fit the PDF to all recorded data points, no uncertainty of this procedure can be extracted in a direct way. To estimate the uncertainties of measured quantities, we therefore implement a bootstrapping approach, assuming our data provide a representative sample of the underlying probability distribution. For each interferometer time T , we use all 300 available data points and randomly draw a set of 300 data points with replacement. In addition to the original data, we generate 999 random sets, giving us access to 1000 independent datasets per T , each comprising 300 points. These datasets are then used to obtain the quantities of interest such as the amplitude A or the differential phase θ via least-square fitting methods. Based on the extracted values, we compute mean and standard deviations for each quantity, which are reported in the main body of this article.

To validate the reliability of the bootstrapping procedure, we compare it against randomly generated numerical datasets. We find no substantial difference in the standard deviations between random and bootstrapped datasets.

4.8 Numerical Replication

To investigate properties such as the bias θ_{bias} or the uncertainty $\Delta\theta$ with finer resolution than the experiment with reasonable effort, we resort to a numerical replication of our experiment. For the numerically generated data, we use the amplitude $A_{0,\text{exp}} = 0.824$ and baseline fluctuations $\sigma_{\text{exp}} = 0.063$ extracted from the experimental datasets, setting the mean baseline offset $\mu = 0$, since it corresponds to a translation that can be neglected. Similar to bootstrapping the experimental data, we produce 1000 numerical datasets containing 300 randomly generated values $S_{\pm 1}$ for each phase θ of interest. Here, we drastically increase the sampling of θ compared to the experiment to give access to finer details. Each random value of $S_{\pm 1}$ is computed by sampling a random phase $\phi_0 \in [0, 2\pi)$ and a baseline value $B_{\pm 1}$ drawn from a normal distribution with mean $\mu = 0$ and variance σ_{exp}^2 . We implement the random number generation using the `numpy.random.default_rng.uniform`

and `numpy.random.default_rng.normal` functions of the `numpy` package in `python` (95, 96). By producing 1000 individual datasets, rather than bootstrapping a single set, as it was done with the experimental data, we can check whether a systematic effect is apparent in the bootstrapping procedure itself, which assumes that the experimental sample size is sufficient to describe the underlying PDF. In our case, we find no systematic difference between the bootstrapped experimental data and numerically generated random data, hence we observe no systematic effects.

4.9 Origin of Bias in PEAC

We identified three main challenges that cause a bias in PEAC: (i) the signal's amplitude A becomes comparable to the standard deviation of the baseline fluctuations σ ; (ii) the true amplitude is close to the fit boundaries; and (iii) resolution limits imposed by bin size. In contrast to ellipse fits at the points of degeneracy, where the algebraic structure reduces to a line and fitting data to an ellipse is ill-posed, the underlying PDF used in PEAC is correct for all differential phases. Thus, the observed bias is not intrinsic to PEAC, but reflects limitations of any fit procedure in regimes of ambiguous parameters, parameters close to boundaries, or a finite resolution.

Addressing (i): Due to the amplitude modulation, the PDF of the histogram transitions from a double-peak to a single-peak distribution, as the two maxima begin to overlap until only one maximum remains, depending on the differential phase. Although no analytical form exists for this transition, we numerically found a threshold at $A/\sigma \cong 1.7777$. Below this limit, two equally plausible fits are possible because of the ambiguity in the combination of A and σ . This ambiguity leads to a wider spread in the amplitude values A , resulting in a wider spread of θ_{rec} and by that increasing its uncertainty $\Delta\theta$. Consequently, the true amplitude value becomes less likely, resulting in a distorted distribution overestimating the mean. A maximum likelihood estimation (83) instead or a Bayesian inference strategy (17, 51, 82) could in principle be used to mitigate this issue.

Addressing (ii): To ensure consistency between $S_{\pm 1}$ and $S_{\text{sum}}, S_{\text{diff}}$, we impose the fit limits $A_{\text{sum}}, A_{\text{diff}} \in [0, \sqrt{2}A_0]$. For example, the upper limit guarantees that a phase reconstruction via Eq. (5) is possible, as higher amplitudes imply values outside the domain of the \arccos function. However, this constrain leads to a truncated distribution of fit parameters, whose mean underestimates the true amplitude value. Over- and underestimating is a general limitation of any fit routine

with physical or logical bounds of the fit parameters.

Addressing (iii): We use a fixed number of 18 bins, but the range of signal values S_{sum} and S_{diff} changes with the differential phase θ because of the modulation of A_{sum} and A_{diff} . A wider range of values implies bigger bin sizes reducing the fit resolution. In combination with (ii), this effect is most likely the reason that the bias in the difference signal (along the major axis) is bigger than the bias in the sum signal (along the minor axis) at $\theta = \pi$.

References and Notes

1. L. Morel, Z. Yao, P. Cladé, S. Guellati-Khélifa, Determination of the fine-structure constant with an accuracy of 81 parts per trillion. *Nature* **588** (7836), 61–65 (2020), doi:10.1038/s41586-020-2964-7, <https://doi.org/10.1038/s41586-020-2964-7>.
2. R. H. Parker, C. Yu, W. Zhong, B. Estey, H. Müller, Measurement of the fine-structure constant as a test of the Standard Model. *Science* **360** (6385), 191–195 (2018), doi:10.1126/science.aap7706, <https://www.science.org/doi/abs/10.1126/science.aap7706>.
3. A. Arvanitaki, P. W. Graham, J. M. Hogan, S. Rajendran, K. Van Tilburg, Search for light scalar dark matter with atomic gravitational wave detectors. *Phys. Rev. D* **97**, 075020 (2018), doi:10.1103/PhysRevD.97.075020, <https://link.aps.org/doi/10.1103/PhysRevD.97.075020>.
4. D. Derr, E. Giese, Clock transitions versus Bragg diffraction in atom-interferometric dark-matter detection. *AVS Quantum Sci.* **5** (4), 044404 (2023), doi:10.1116/5.0176666, <https://doi.org/10.1116/5.0176666>.
5. S. Abend, *et al.*, Terrestrial very-long-baseline atom interferometry: Workshop summary. *AVS Quantum Sci.* **6** (2), 024701 (2024), doi:10.1116/5.0185291, <https://doi.org/10.1116/5.0185291>.
6. A. Abdalla, *et al.*, Terrestrial Very-Long-Baseline Atom Interferometry: summary of the second workshop. *EPJ Quantum Technol.* **12** (1), 42 (2025), doi:10.1140/epjqt/s40507-025-00344-3, <https://doi.org/10.1140/epjqt/s40507-025-00344-3>.
7. G. Rosi, F. Sorrentino, L. Cacciapuoti, M. Prevedelli, G. M. Tino, Precision measurement of the Newtonian gravitational constant using cold atoms. *Nature* **510** (7506), 518–521 (2014), doi:10.1038/nature13433, <https://doi.org/10.1038/nature13433>.
8. G. Lamporesi, A. Bertoldi, L. Cacciapuoti, M. Prevedelli, G. M. Tino, Determination of the Newtonian Gravitational Constant Using Atom Interferometry. *Phys. Rev. Lett.* **100**, 050801 (2008), doi:10.1103/PhysRevLett.100.050801, <https://link.aps.org/doi/10.1103/PhysRevLett.100.050801>.

9. J. B. Fixler, G. T. Foster, J. M. McGuirk, M. A. Kasevich, Atom Interferometer Measurement of the Newtonian Constant of Gravity. *Science* **315** (5808), 74–77 (2007), doi:10.1126/science.1135459, <https://www.science.org/doi/abs/10.1126/science.1135459>.
10. I. Pikovski, M. Zych, F. Costa, Č. Brukner, Universal decoherence due to gravitational time dilation. *Nature Phys.* **11** (8), 668–672 (2015), doi:10.1038/nphys3366, <https://doi.org/10.1038/nphys3366>.
11. D. Schlippert, *et al.*, Quantum Test of the Universality of Free Fall. *Phys. Rev. Lett.* **112**, 203002 (2014), doi:10.1103/PhysRevLett.112.203002, <https://link.aps.org/doi/10.1103/PhysRevLett.112.203002>.
12. P. Asenbaum, C. Overstreet, M. Kim, J. Curti, M. A. Kasevich, Atom-Interferometric Test of the Equivalence Principle at the 10^{-12} Level. *Phys. Rev. Lett.* **125**, 191101 (2020), doi:10.1103/PhysRevLett.125.191101, <https://link.aps.org/doi/10.1103/PhysRevLett.125.191101>.
13. B. Barrett, *et al.*, Dual matter-wave inertial sensors in weightlessness. *Nat. Commun.* **7** (1), 13786 (2016), doi:10.1038/ncomms13786, <https://doi.org/10.1038/ncomms13786>.
14. S. Schaffrath, D. Störk, F. Di Pumbo, E. Giese, Unified laboratory-frame analysis of atomic gravitational-wave sensors. *AVS Quantum Sci.* **7** (4), 044402 (2025), doi:10.1116/5.0304468, <https://doi.org/10.1116/5.0304468>.
15. N. Yu, M. Tinto, Gravitational wave detection with single-laser atom interferometers. *Gen. Relativ. Gravitation* **43** (7), 1943–1952 (2011), doi:10.1007/s10714-010-1055-8, <https://doi.org/10.1007/s10714-010-1055-8>.
16. W. Chaibi, *et al.*, Low frequency gravitational wave detection with ground-based atom interferometer arrays. *Phys. Rev. D* **93**, 021101 (2016), doi:10.1103/PhysRevD.93.021101, <https://link.aps.org/doi/10.1103/PhysRevD.93.021101>.
17. B. Barrett, *et al.*, Correlative methods for dual-species quantum tests of the weak equivalence principle. *New J. Phys.* **17** (8), 085010 (2015), doi:10.1088/1367-2630/17/8/085010, <https://doi.org/10.1088/1367-2630/17/8/085010>.

18. B. Barrett, *et al.*, Testing the universality of free fall using correlated ^{39}K – ^{87}Rb atom interferometers. *AVS Quantum Sci.* **4** (1), 014401 (2022), doi:10.1116/5.0076502, <https://doi.org/10.1116/5.0076502>.
19. K. Bongs, *et al.*, Taking atom interferometric quantum sensors from the laboratory to real-world applications. *Nat. Rev. Phys.* **1** (12), 731–739 (2019), doi:10.1038/s42254-019-0117-4, <https://doi.org/10.1038/s42254-019-0117-4>.
20. E. R. Elliott, *et al.*, Quantum gas mixtures and dual-species atom interferometry in space. *Nature* **623** (7987), 502–508 (2023), doi:10.1038/s41586-023-06645-w, <https://doi.org/10.1038/s41586-023-06645-w>.
21. M. Meister, *et al.*, Space magnetometry with a differential atom interferometer (2025), <https://arxiv.org/abs/2505.23532>.
22. K. S. Hardman, *et al.*, Simultaneous Precision Gravimetry and Magnetic Gradiometry with a Bose-Einstein Condensate: A High Precision, Quantum Sensor. *Phys. Rev. Lett.* **117**, 138501 (2016), doi:10.1103/PhysRevLett.117.138501, <https://link.aps.org/doi/10.1103/PhysRevLett.117.138501>.
23. M.-K. Zhou, *et al.*, Precisely mapping the magnetic field gradient in vacuum with an atom interferometer. *Phys. Rev. A* **82**, 061602 (2010), doi:10.1103/PhysRevA.82.061602, <https://link.aps.org/doi/10.1103/PhysRevA.82.061602>.
24. Z.-K. Hu, *et al.*, Simultaneous differential measurement of a magnetic-field gradient by atom interferometry using double fountains. *Phys. Rev. A* **84**, 013620 (2011), doi:10.1103/PhysRevA.84.013620, <https://link.aps.org/doi/10.1103/PhysRevA.84.013620>.
25. T. L. Gustavson, A. Landragin, M. A. Kasevich, Rotation sensing with a dual atom-interferometer Sagnac gyroscope. *Classical Quantum Gravity* **17** (12), 2385 (2000), doi:10.1088/0264-9381/17/12/311, <https://doi.org/10.1088/0264-9381/17/12/311>.
26. P. Berg, *et al.*, Composite-Light-Pulse Technique for High-Precision Atom Interferometry. *Phys. Rev. Lett.* **114**, 063002 (2015), doi:10.1103/PhysRevLett.114.063002, <https://link.aps.org/doi/10.1103/PhysRevLett.114.063002>.

27. B. Canuel, *et al.*, Six-Axis Inertial Sensor Using Cold-Atom Interferometry. *Phys. Rev. Lett.* **97**, 010402 (2006), doi:10.1103/PhysRevLett.97.010402, <https://link.aps.org/doi/10.1103/PhysRevLett.97.010402>.

28. M. M. Beydler, E. R. Moan, Z. Luo, Z. Chu, C. A. Sackett, Guided-wave Sagnac atom interferometer with large area and multiple orbits. *AVS Quantum Sci.* **6** (1), 014401 (2024), doi:10.1116/5.0173769, <https://doi.org/10.1116/5.0173769>.

29. F. Sorrentino, *et al.*, Sensitivity limits of a Raman atom interferometer as a gravity gradiometer. *Phys. Rev. A* **89**, 023607 (2014), doi:10.1103/PhysRevA.89.023607, <https://link.aps.org/doi/10.1103/PhysRevA.89.023607>.

30. M. J. Snadden, J. M. McGuirk, P. Bouyer, K. G. Haritos, M. A. Kasevich, Measurement of the Earth's Gravity Gradient with an Atom Interferometer-Based Gravity Gradiometer. *Phys. Rev. Lett.* **81**, 971–974 (1998), doi:10.1103/PhysRevLett.81.971, <https://link.aps.org/doi/10.1103/PhysRevLett.81.971>.

31. A. Bertoldi, *et al.*, Atom interferometry gravity-gradiometer for the determination of the Newtonian gravitational constant G. *Eur. Phys. J. D* **40** (2), 271–279 (2006), doi:10.1140/epjd/e2006-00212-2, <https://doi.org/10.1140/epjd/e2006-00212-2>.

32. S. M. Dickerson, J. M. Hogan, A. Sugarbaker, D. M. S. Johnson, M. A. Kasevich, Multiaxis Inertial Sensing with Long-Time Point Source Atom Interferometry. *Phys. Rev. Lett.* **111**, 083001 (2013), doi:10.1103/PhysRevLett.111.083001, <https://link.aps.org/doi/10.1103/PhysRevLett.111.083001>.

33. G. T. Foster, J. B. Fixler, J. M. McGuirk, M. A. Kasevich, Method of phase extraction between coupled atom interferometers using ellipse-specific fitting. *Opt. Lett.* **27** (11), 951 (2002), doi:10.1364/ol.27.000951.

34. X. Zhang, *et al.*, Dependence of the ellipse fitting noise on the differential phase between interferometers in atom gravity gradiometers. *Opt. Express* **31** (26), 44102–44112 (2023), doi:10.1364/OE.507695, <https://opg.optica.org/oe/abstract.cfm?URI=oe-31-26-44102>.

35. A. Fitzgibbon, M. Pilu, R. Fisher, Direct least square fitting of ellipses. *IEEE Transactions on Pattern Analysis and Machine Intelligence* **21** (5), 476–480 (1999), doi:10.1109/34.765658.

36. Z. L. Szpak, W. Chojnacki, A. van den Hengel, Guaranteed Ellipse Fitting with the Sampson Distance, in *Computer Vision – ECCV 2012*, A. Fitzgibbon, S. Lazebnik, P. Perona, Y. Sato, C. Schmid, Eds. (Springer Berlin Heidelberg, Berlin, Heidelberg) (2012), pp. 87–100.

37. Joint Committee for Guides in Metrology, International Vocabulary of Metrology – Basic and general concepts and associated terms (VIM), 3rd edition, JCGM 200:2012 (2012), doi: 10.59161/JCGM200-2012, <https://doi.org/10.59161/JCGM200-2012>.

38. Accuracy (trueness and precision) of measurement methods and results — Part 1: General principles and definitions (2023), <https://www.iso.org/obp/ui/#iso:std:iso:5725:-1:ed-2:v1:en>, 2nd edition, July 2023.

39. A. Roura, Gravitational Redshift in Quantum-Clock Interferometry. *Phys. Rev. X* **10**, 021014 (2020), doi:10.1103/PhysRevX.10.021014, <https://link.aps.org/doi/10.1103/PhysRevX.10.021014>.

40. F. Di Pumbo, *et al.*, Gravitational Redshift Tests with Atomic Clocks and Atom Interferometers. *PRX Quantum* **2**, 040333 (2021), doi:10.1103/PRXQuantum.2.040333, <https://link.aps.org/doi/10.1103/PRXQuantum.2.040333>.

41. G. Rosi, *et al.*, Quantum test of the equivalence principle for atoms in coherent superposition of internal energy states. *Nat. Commun.* **8** (1), 15529 (2017), doi:10.1038/ncomms15529, <https://doi.org/10.1038/ncomms15529>.

42. J. Borregaard, I. Pikovski, Testing quantum theory on curved spacetime with quantum networks. *Phys. Rev. Res.* **7**, 023192 (2025), doi:10.1103/PhysRevResearch.7.023192, <https://link.aps.org/doi/10.1103/PhysRevResearch.7.023192>.

43. C. Fromontiel, *et al.*, Non-local mass superpositions and optical clock interferometry in atomic ensemble quantum networks (2025), <https://arxiv.org/abs/2509.19501>.

44. M. Gündoğan, R. Barzel, D. Rätzel, Gravitational time dilation in quantum clock interferometry with entangled multi-photon states and quantum memories. *arXiv* (2026), <https://doi.org/10.48550/arXiv.2601.02470>.
45. M. Zych, F. Costa, I. Pikovski, Č. Brukner, Quantum interferometric visibility as a witness of general relativistic proper time. *Nat. Commun.* **2** (1), 505 (2011), doi:10.1038/ncomms1498, <https://doi.org/10.1038/ncomms1498>.
46. J. P. Covey, I. Pikovski, J. Borregaard, Probing Curved Spacetime with a Distributed Atomic Processor Clock. *PRX Quantum* **6**, 030310 (2025), doi:10.1103/q188-b1cr, <https://link.aps.org/doi/10.1103/q188-b1cr>.
47. S. Loriani, *et al.*, Interference of clocks: A quantum twin paradox. *Sci. Adv.* **5** (10), eaax8966 (2019), doi:10.1126/sciadv.aax8966, <https://www.science.org/doi/abs/10.1126/sciadv.aax8966>.
48. Y. Margalit, *et al.*, A self-interfering clock as a “which path” witness. *Science* **349** (6253), 1205–1208 (2015), doi:10.1126/science.aac6498, <https://www.science.org/doi/abs/10.1126/science.aac6498>.
49. R. Geiger, *et al.*, Detecting inertial effects with airborne matter-wave interferometry. *Nat. Commun.* **2** (1), 474 (2011), doi:10.1038/ncomms1479, <https://doi.org/10.1038/ncomms1479>.
50. S. Abend, *et al.*, Atom-Chip Fountain Gravimeter. *Phys. Rev. Lett.* **117**, 203003 (2016), doi:10.1103/PhysRevLett.117.203003, <https://link.aps.org/doi/10.1103/PhysRevLett.117.203003>.
51. C. Pelluet, *et al.*, Atom interferometry in an Einstein Elevator. *Nat. Commun.* **16** (1), 4812 (2025), doi:10.1038/s41467-025-60042-7, <https://doi.org/10.1038/s41467-025-60042-7>.
52. Z. Zhou, S. C. Carrasco, C. Sanner, V. S. Malinovsky, R. Folman, Geometric phase amplification in a clock interferometer for enhanced metrology. *Sci. Adv.* **11** (18), eadr6893 (2025), doi:10.1126/sciadv.adr6893, <https://www.science.org/doi/abs/10.1126/sciadv.adr6893>.
53. X. Zheng, J. Dolde, M. C. Cambria, H. M. Lim, S. Kolkowitz, A lab-based test of the gravitational redshift with a miniature clock network. *Nat. Commun.* **14** (1), 4886 (2023), doi:10.1038/s41467-023-40629-8, <https://doi.org/10.1038/s41467-023-40629-8>.

54. T. Bothwell, *et al.*, Resolving the gravitational redshift across a millimetre-scale atomic sample. *Nature* **602** (7897), 420–424 (2022), doi:10.1038/s41586-021-04349-7, <https://doi.org/10.1038/s41586-021-04349-7>.

55. C. Struckmann, *et al.*, Platform and environment requirements of a satellite quantum test of the weak equivalence principle at the 10^{-17} level. *Phys. Rev. D* **109**, 064010 (2024), doi: 10.1103/PhysRevD.109.064010, <https://link.aps.org/doi/10.1103/PhysRevD.109.064010>.

56. S. Hartmann, *et al.*, Regimes of atomic diffraction: Raman versus Bragg diffraction in retroreflective geometries. *Phys. Rev. A* **101**, 053610 (2020), doi:10.1103/PhysRevA.101.053610, <https://link.aps.org/doi/10.1103/PhysRevA.101.053610>.

57. T. Lauber, J. Küber, O. Wille, G. Birkl, Optimized Bose-Einstein-condensate production in a dipole trap based on a 1070-nm multifrequency laser: Influence of enhanced two-body loss on the evaporation process. *Phys. Rev. A* **84** (4), 043641 (2011), doi:10.1103/PhysRevA.84.043641, <https://link.aps.org/doi/10.1103/PhysRevA.84.043641>.

58. D. Pfeiffer, M. Dietrich, P. Schach, G. Birkl, E. Giese, Dichroic mirror pulses for optimized higher-order atomic Bragg diffraction. *Phys. Rev. Res.* **7**, L012028 (2025), doi:10.1103/PhysRevResearch.7.L012028, <https://link.aps.org/doi/10.1103/PhysRevResearch.7.L012028>.

59. R. B. Blackman, J. W. Tukey, The Measurement of Power Spectra from the Point of View of Communications Engineering — Part I. *Bell System Technical Journal* **37** (1), 185–282 (1958), doi:<https://doi.org/10.1002/j.1538-7305.1958.tb03874.x>, <https://onlinelibrary.wiley.com/doi/abs/10.1002/j.1538-7305.1958.tb03874.x>.

60. E. Weisstein, Blackman Function, *MathWorld*—A Wolfram Resource, <https://mathworld.wolfram.com/BlackmanFunction.html>.

61. S.-w. Chiow, T. Kovachy, H.-C. Chien, M. A. Kasevich, $102\hbar k$ Large Area Atom Interferometers. *Phys. Rev. Lett.* **107**, 130403 (2011), doi:10.1103/PhysRevLett.107.130403, <https://link.aps.org/doi/10.1103/PhysRevLett.107.130403>.

62. T. Berrada, *et al.*, Integrated Mach–Zehnder interferometer for Bose–Einstein condensates. *Nat. Commun.* **4** (1), 2077 (2013), doi:10.1038/ncomms3077, <https://doi.org/10.1038/ncomms3077>.

63. A. Bertoldi, F. Minardi, M. Prevedelli, Phase shift in atom interferometers: Corrections for nonquadratic potentials and finite-duration laser pulses. *Phys. Rev. A* **99**, 033619 (2019), doi: 10.1103/PhysRevA.99.033619, <https://link.aps.org/doi/10.1103/PhysRevA.99.033619>.

64. W. Gerlach, O. Stern, *Der experimentelle Nachweis der Richtungsquantelung im Magnetfeld* (Springer Berlin Heidelberg, Berlin, Heidelberg), pp. 26–29 (1989), doi:10.1007/978-3-642-74813-4_4, https://doi.org/10.1007/978-3-642-74813-4_4.

65. M. Bauer, The Stern-Gerlach Experiment, Translation of: “Der experimentelle Nachweis der Richtungsquantelung im Magnetfeld” (2023), <https://arxiv.org/abs/2301.11343>.

66. B. Efron, R. J. Tibshirani, *An introduction to the bootstrap* (Chapman and Hall/CRC) (1994).

67. B. Efron, The Bootstrap and Modern Statistics. *J. Am. Stat. Assoc.* **95** (452), 1293–1296 (2000), doi:10.1080/01621459.2000.10474333, <https://www.tandfonline.com/doi/abs/10.1080/01621459.2000.10474333>.

68. A. Zoubir, B. Boashash, The bootstrap and its application in signal processing. *IEEE Signal Processing Magazine* **15** (1), 56–76 (1998), doi:10.1109/79.647043.

69. G. Rosi, *et al.*, Measurement of the Gravity-Field Curvature by Atom Interferometry. *Phys. Rev. Lett.* **114**, 013001 (2015), doi:10.1103/PhysRevLett.114.013001, <https://link.aps.org/doi/10.1103/PhysRevLett.114.013001>.

70. X. Jiang, D.-C. Cheng, Fitting of 3D circles and ellipses using a parameter decomposition approach, in *Fifth International Conference on 3-D Digital Imaging and Modeling (3DIM’05)* (2005), pp. 103–109, doi:10.1109/3DIM.2005.46.

71. S.-w. Chiow, S. Herrmann, S. Chu, H. Müller, Noise-Immune Conjugate Large-Area Atom Interferometers. *Physical Review Letters* **103** (5), 050402 (2009), doi:10.1103/PhysRevLett.103.050402, <https://link.aps.org/doi/10.1103/PhysRevLett.103.050402>.

72. R. Halır, J. Flusser, Numerically stable direct least squares fitting of ellipses, in *Proc. 6th International Conference in Central Europe on Computer Graphics and Visualization. WSCG* (Citeseer), vol. 98 (1998), pp. 125–132.

73. C. Hill, Ellipse Fitting Algorithm, scipython.com, <https://scipython.com/blog/direct-linear-least-squares-fitting-of-an-ellipse/>.

74. K. Ridley, A. Rodgers, An investigation of errors in ellipse-fitting for cold-atom interferometers. *EPJ Quantum Technol.* **11** (1), 79 (2024), doi:10.1140/epjqt/s40507-024-00292-4, <https://doi.org/10.1140/epjqt/s40507-024-00292-4>.

75. W. Gander, G. H. Golub, R. Strebel, Least-squares fitting of circles and ellipses. *BIT* **34** (4), 558–578 (1994), doi:10.1007/bf01934268, <https://doi.org/10.1007/BF01934268>.

76. S. J. Ahn, W. Rauh, H.-J. Warnecke, Least-squares orthogonal distances fitting of circle, sphere, ellipse, hyperbola, and parabola. *Pattern Recognit.* **34** (12), 2283–2303 (2001), doi:10.1016/S0031-3203(00)00152-7, <https://www.sciencedirect.com/science/article/pii/S0031320300001527>.

77. X. Chen, *et al.*, Proportional-scanning-phase method to suppress the vibrational noise in non-isotope dual-atom-interferometer-based weak-equivalence-principle-test experiments. *Phys. Rev. A* **90**, 023609 (2014), doi:10.1103/PhysRevA.90.023609, <https://link.aps.org/doi/10.1103/PhysRevA.90.023609>.

78. H. Müller, S.-w. Chiow, Q. Long, S. Herrmann, S. Chu, Atom Interferometry with up to 24-Photon-Momentum-Transfer Beam Splitters. *Phys. Rev. Lett.* **100**, 180405 (2008), doi:10.1103/PhysRevLett.100.180405, <https://link.aps.org/doi/10.1103/PhysRevLett.100.180405>.

79. T. Kovachy, *et al.*, Quantum superposition at the half-metre scale. *Nature* **528** (7583), 530–533 (2015), doi:10.1038/nature16155, <https://doi.org/10.1038/nature16155>.

80. Q. d'Armagnac de Castanet, *et al.*, Atom interferometry at arbitrary orientations and rotation rates. *Nat. Commun.* **15** (1), 6406 (2024), doi:10.1038/s41467-024-50804-0, <https://doi.org/10.1038/s41467-024-50804-0>.

81. S. Otabe, *et al.*, Sensitivity Enhancement in Atom-Interferometer Gyroscopes via Phase-Modulation Signal Readout Scheme (2025), <https://arxiv.org/abs/2506.23250>.

82. J. K. Stockton, X. Wu, M. A. Kasevich, Bayesian estimation of differential interferometer phase. *Phys. Rev. A* **76**, 033613 (2007), doi:10.1103/PhysRevA.76.033613, <https://link.aps.org/doi/10.1103/PhysRevA.76.033613>.

83. L. Pezzè, A. Santoni, C. Mazzinghi, M. Fattori, A. Smerzi, Joint estimation of phase and uncorrelated dephasing in a differential quantum interferometer (2025), <https://arxiv.org/abs/2503.18166>.

84. R. Corgier, *et al.*, Optimized squeezing for accurate differential sensing under large phase noise. *Quantum Sci. Technol.* **10** (4), 045016 (2025), doi:10.1088/2058-9565/adf2d8, <https://doi.org/10.1088/2058-9565/adf2d8>.

85. D. Pfeiffer, *Novel Techniques for Atom Trapping and Large-Momentum-Transfer Atom Interferometry*, Dissertation, Technische Universität Darmstadt, Darmstadt (2025), doi:<https://doi.org/10.26083/tuprints-00031145>, <https://tuprints.ulb.tu-darmstadt.de/handle/tuda/14381>.

86. W. Ketterle, D. S. Durfee, D. M. Stamper-Kurn, Making, probing and understanding Bose-Einstein condensates. *arXiv* (1999), <https://doi.org/10.48550/arXiv.cond-mat/9904034>.

87. C. Antoine, Matter wave beam splitters in gravito-inertial and trapping potentials: generalized ttt scheme for atom interferometry. *Appl. Phys. B* **84** (4), 585–597 (2006), doi:10.1007/s00340-006-2378-8, <https://doi.org/10.1007/s00340-006-2378-8>.

88. X. Li, C.-G. Shao, Z.-K. Hu, Raman pulse duration effect in high-precision atom interferometry gravimeters. *J. Opt. Soc. Am. B* **32** (2), 248–257 (2015), doi:10.1364/JOSAB.32.000248, <https://opg.optica.org/josab/abstract.cfm?URI=josab-32-2-248>.

89. A. Bott, F. Di Pumbo, E. Giese, Atomic diffraction from single-photon transitions in gravity and Standard-Model extensions. *AVS Quantum Sci.* **5** (4), 044402 (2023), doi:10.1116/5.0174258, <https://doi.org/10.1116/5.0174258>.

90. E. Weisstein, Harmonic Addition Theorem, *MathWorld—A Wolfram Resource*, <https://mathworld.wolfram.com/HarmonicAdditionTheorem.html>.
91. H. Shimazaki, S. Shinomoto, A Method for Selecting the Bin Size of a Time Histogram. *Neural Comput.* **19** (6), 1503–1527 (2007), doi:10.1162/neco.2007.19.6.1503, <https://doi.org/10.1162/neco.2007.19.6.1503>.
92. H. O. Lohaka, *Making a Grouped-data Frequency Table: Development and Examination of the Iteration Algorithm*, Ph.D. thesis, Ohio University (2007), https://etd.ohiolink.edu/acprod/odb_etd/ws/send_file/send?accession=ohiou1194981215.
93. R. Chattamvelli, R. Shanmugam, Arcsine Distribution, in *Continuous Distributions in Engineering and the Applied Sciences-Part I* (Springer), pp. 57–68 (2021), doi:doi.org/10.1007/978-3-031-02430-6_5, https://doi.org/10.1007/978-3-031-02430-6_5.
94. P. Virtanen, *et al.*, SciPy 1.0: Fundamental Algorithms for Scientific Computing in Python. *Nature Methods* **17**, 261–272 (2020), doi:10.1038/s41592-019-0686-2.
95. C. R. Harris, *et al.*, Array programming with NumPy. *Nature* **585** (7825), 357–362 (2020), doi:10.1038/s41586-020-2649-2, <https://doi.org/10.1038/s41586-020-2649-2>.
96. Python Software Foundation, Python Language Reference, version 3.12 (2026), <https://docs.python.org/3/reference/>.

Acknowledgments

We thank S. Abend, F. Di Pumo, A. Friedrich, S. Kanthak, M. Meister, and D. Reinhard for stimulating discussions and suggestions. We acknowledge contributions from the Terrestrial Very-Long-Baseline Atom Interferometry (TVLBAI) proto-collaboration.

Funding: The QUANTUS-VI project is supported by the German Space Agency at the German Aerospace Center (Deutsche Raumfahrtagentur im Deutschen Zentrum für Luft- und Raumfahrt, DLR) with funds provided by the Federal Ministry for Economic Affairs and Climate Action (Bundesministerium für Wirtschaft und Klimaschutz, BMWK) due to an enactment of the German Bundestag under grant no. 50WM2450E (QUANTUS-VI).

Author contributions: Conceptualisation: EG, GB, DD (supporting), DP (supporting); Data curation: DD, DP, LL (supporting); Formal analysis: DD, DP, LL (supporting); Funding acquisition: EG, GB; Investigation: DD, DP, LL (supporting); Methodology: DD, DP, EG (supporting), GB (supporting); Software: DD, DP, LL (supporting); Supervision: EG, GB; Validation: DD, DP, LL, EG, GB; Visualisation: DD, DP, EG (supporting), GB (supporting); Writing – original draft: DD, DP, EG (supporting); Writing – review & editing: DD, DP, EG, GB, LL (supporting)

Competing interests: There are no competing interests to declare.